Fast Na⁺ Kinetics and Suppressed Voltage Hysteresis Enabled by a High-Entropy Strategy for Sodium Oxide Cathodes

Xian-Zuo Wang, Yuting Zuo, Yuanbin Qin, Xu Zhu, Shao-Wen Xu, Yu-Jie Guo, Tianran Yan, Liang Zhang, Zhibin Gao,* Lianzheng Yu, Mengting Liu, Ya-Xia Yin, Yonghong Cheng,* Peng-Fei Wang,* and Yu-Guo Guo*

O3-type layered transition metal cathodes are promising energy storage materials due to their sufficient sodium reservoir. However, sluggish sodium ions kinetics and large voltage hysteresis, which are generally associated with Na⁺ diffusion properties and electrochemical phase transition reversibility, drastically minimize energy density, reduce energy efficiency, and hinder further commercialization of sodium-ion batteries (SIBs). Here, this work proposes a high-entropy tailoring strategy through manipulating the electronic local environment within transition metal slabs to circumvent these issues. Experimental analysis combined with theoretical calculations verify that high-entropy metal ion mixing contributes to the improved reversibility of redox reaction and O3–P3–O3 phase transition behaviors as well as the enhanced Na⁺ diffusivity. Consequently, the designed O3-Na$_{0.9}$Ni$_{0.2}$Fe$_{0.2}$Co$_{0.2}$Mn$_{0.2}$Ti$_{0.15}$Cu$_{0.05}$O$_2$ material with high-entropy characteristic could display a negligible voltage hysteresis (<0.09 V), impressive rate capability (98.6 mAh g⁻¹ at 10 C) and long-term cycling stability (79.4% capacity retention over 2000 cycles at 5 C). This work provides insightful guidance in mitigating the voltage hysteresis and facilitating Na⁺ diffusion of layered oxide cathode materials to realize high-rate and high-energy SIBs.

1. Introduction

Sodium-ion batteries (SIBs) have attracted increasing attention as a new type of energy storage technology in recent years.[1] Compared with commonly used lithium-ion batteries, SIBs own advantages such as abundant raw material reserves and low cost, making them suitable for sustainable development of large-scale energy storage and low-speed electric vehicle fields.[2] However, the extraction/insertion of large-sized Na ions (1.02 Å) accompanied with the change of electronic structure in electrode materials inevitably leads to their irreversible structure changes, thus it is crucial to find suitable cathode material hosts toward the practical application of SIBs.[3] Among various cathode candidates, layered transition metal oxides (Na$_x$TMO$_2$, TM = transition metals), which are categorized by typical P2 structure (Na⁺ in prismatic sites) and O3 phase (Na⁺ in octahedral

X.-Z. Wang, Y. Zuo, X. Zhu, S.-W. Xu, L. Yu, M. Liu, Y. Cheng, P.-F. Wang
Center of Nanomaterials for Renewable Energy
State Key Laboratory of Electrical Insulation and Power Equipment
School of Electrical Engineering
Xi'an Jiaotong University
Xi'an, Shaanxi 710049, P. R. China
E-mail: cyh@xjtu.edu.cn; pfwang@xjtu.edu.cn

Y. Zuo, Z. Gao
State Key Laboratory for Mechanical Behavior of Materials
School of Materials Science and Engineering
Xi'an Jiaotong University
Xi'an, Shaanxi 710049, P. R. China
E-mail: zhibin.gao@xjtu.edu.cn

Y. Qin
Center for Advancing Materials Performance from the Nanoscale (CAMP-Nano)
State Key Laboratory for Mechanical Behavior of Materials
Xi'an Jiaotong University
Xi'an, Shaanxi 710049, P. R. China

Y.-J. Guo, Y.-X. Yin, Y.-G. Guo
CAS Key Laboratory of Molecular Nanostructure and Nanotechnology
CAS Research/Education Center for Excellence in Molecular Sciences
Beijing National Laboratory for Molecular Sciences
Institute of Chemistry
Chinese Academy of Sciences (CAS)
Beijing 100190, P. R. China
E-mail: ygguo@iccas.ac.cn

Y.-J. Guo, Y.-X. Yin, Y.-G. Guo
School of Chemical Sciences
University of Chinese Academy of Sciences
Beijing 100049, P. R. China

T. Yan, L. Zhang
Institute of Functional Nano & Soft Materials (FUNSOM)
Jiangsu Key Laboratory of Advanced Negative Carbon Technologies
Soochow University
Suzhou, Jiangsu 215123, P. R. China

L. Yu, P.-F. Wang
Jiangsu Jufeng New Energy Technology Co. Ltd.
Changzhou, Jiangsu 213166, P. R. China

sites), are considered promising choices because of their simple manufacturing process and excellent electrochemical activity.[4] Compared with P2 counterparts, O3-type layered oxide materials own an adequate initial sodium content with high initial Coulombic efficiency and theoretical specific capacity, making them more suitable for application in full cells.[5]

Although demonstrating a high capacity, application-wise, O3-type oxide materials remain several formidable issues to be further resolved. First, complicated phase transitions accompanied by sluggish sodium ions diffusion kinetics frequently occurred during repeated Na^+ extraction/insertion process, leading to unsatisfactory capacity retention and poor rate performance.[6] Previous studies showed partial metal substitution in bulk such as Ti^{4+},[7] Cu^{2+},[8] and Fe^{3+}.[9] are demonstrated effective to simplify the complex phase evolution. However, for most O3-type layered materials, the phase transition between O3 and P3 still exists within the voltage region near 3 V.[10] The sodium kinetics are closely linked with the electrochemical O3–P3–O3 phase transformation process, which drastically affects rate capability of SIBs. In addition, because the voltage related to this redox process upon Na^+ extraction cannot be recovered after Na^+ intercalation, large voltage hysteresis and significant loss of energy density are undoubtedly another challenge that prohibits exploiting the full potential of O3 materials.[11] Currently, voltage hysteresis was mainly discovered in Li-rich materials[12] and some P2 materials with anionic redox,[13] while research on voltage hysteresis phenomenon is rarely reported for O3-type materials. Since voltage hysteresis persists throughout the overall electrochemical cycling, the average discharge voltage showed a continuous decrease, which is called voltage decay or voltage fade.[14] Voltage hysteresis accompanied by cumulative voltage decay not only reduces energy efficiency and drastically minimizes energy density, but also hinders further commercialization of SIBs.[15] Therefore, synchronously addressing the sluggish sodium kinetics and serious voltage hysteresis issues is of great significance for developing high-energy and high-rate O3-type layered oxide cathode materials.

Recently, the proposal of high-entropy oxides (HEOs) might provide guidance in solving the above problems.[16] The concept of high-entropy originated from high-entropy alloys (HEAs), which have a series of excellent properties compared to traditional alloys, such as high fracture toughness with high strength in mechanical properties, and good energy storage performance in thermodynamics.[17] Recent reports of sodium HEOs ($Na_{0.95}Li_{0.07}Cu_{0.11}Ni_{0.11}Fe_{0.3}Mn_{0.41}O_{1.97}F_{0.03}$,[18] $Na_{0.83}Li_{0.1}Ni_{0.25}Co_{0.2}Mn_{0.15}Ti_{0.15}Sn_{0.15}O_{2-\delta}$,[19] $NaNi_{0.25}Mg_{0.05}Cu_{0.1}Fe_{0.2}Mn_{0.2}Ti_{0.1}Sn_{0.1}O_2$,[20] etc.) proposed that the host matrix was stabilized by entropy effect, leading to enhanced electrochemical performance as well as thermal stability. For instance, $NaNi_{1/4}Co_{1/4}Fe_{1/4}Mn_{1/8}Ti_{1/8}O_2$ delivered capacity stabilized at 96.82 mAh g^{-1} after 100 cycles at 2 C, corresponding to a capacity retention rate of 97.72%.[21] Zhao et al. synthesized O3-type $NaNi_{0.12}Cu_{0.12}Mg_{0.12}Fe_{0.15}Co_{0.15}Mn_{0.1}Ti_{0.1}Sn_{0.1}Sb_{0.04}O_2$ high-entropy layered material, which exhibited a reversible specific capacity of 110 mAh g^{-1} at 0.1 C, and a capacity retention about 90% after 200 cycles at 0.5 C accompanied by O3–P3 phase transition delay.[22] However, the fundamental mechanism especially for reaction kinetics and voltage hysteresis behind the high-entropy effect currently remains controversial and unclear,

which might obstruct further development of state-of-the-art sodium high-entropy cathode materials.

To analyze the entropy effect on the reaction mechanism of cathode materials, we constructed high-entropy configuration in a series of O3-type materials based on $Na_{0.8+0.1x}Ni_{0.2}Fe_{0.2}Co_{0.2}Mn_{0.2}Ti_{0.2-0.05x}Cu_{0.05x}O_2$ model systems, in which $Ni^{2+}/Fe^{3+}/Co^{3+}/Cu^{2+}$ provides charge compensation, Mn^{4+} stabilizes the structural integrity,[23] and Ti^{4+} raises the average voltage,[24] forming $Na_{0.8}Ni_{0.2}Fe_{0.2}Co_{0.2}Mn_{0.2}Ti_{0.2}O_2$ (NaNFCMTC-0), $Na_{0.9}Ni_{0.2}Fe_{0.2}Co_{0.2}Mn_{0.2}Ti_{0.15}Cu_{0.05}O_2$ (NaNFCMTC-1), and $Na_{1.0}Ni_{0.2}Fe_{0.2}Co_{0.2}Mn_{0.2}Ti_{0.1}Cu_{0.1}O_2$ (NaNFCMTC-2). It is demonstrated that this multi-ion synergistic high-entropy layered oxide NaNFCMTC-1 exhibits high-rate performance and negligible voltage decay during long-term cycling, accompanied by highly reversible Ni/Fe/Co/Cu redox and phase transition behaviors between O3 and P3 phase. NaNFCMTC-1 contracts TMO_2 slabs and enlarges Na spacing distance, rendering fast Na^+ transport through an expanded Na^+ octahedral–tetrahedral–octahedral transport channel and low Na^+ migration energy during Na^+ (de)intercalation process.

2. Results and Discussion

For sodium layered oxides, the number of transition metal elements has an important influence on the configurational entropy. Assuming that the stoichiometric ratios of all transition metal elements are equal, and regardless of sodium content and anion content, the relationship between the configurational entropy in transition metal framework and the number of transition metal elements is shown in **Figure 1**a. It is generally considered that the configurational entropy of high-entropy materials is higher than $1.5R$, which means there are five or more elements contained.[25] However, excessive types of cations will increase the difficulty of synthesis, accompanied by impurities and poor crystallinity, leading to deteriorated performance. Moreover, as the number of transition metal elements increases, the trend of configurational entropy gradually slows down. Therefore, blindly pursuing multiple elements to increase configurational entropy is not advisable. So the $Na_{0.8+0.1x}Ni_{0.2}Fe_{0.2}Co_{0.2}Mn_{0.2}Ti_{0.2-0.05x}Cu_{0.05x}O_2$ model system containing five or six transition metal elements with a configurational entropy of 1.60–1.75R is selected for the following study.

To assess the multi-ion synergistic effects resulting from the high-entropy strategy on the electronic structure of NaNFCMTC-1, density functional theory (DFT) calculations were conducted. The calculated partial density of states (PDOS) of transition metals is illustrated in Figure 1b. The contribution of Ti 3d to the density of states (DOS) is predominantly concentrated in the high-energy region above the Fermi energy level (0.9–1.8 eV), suggesting that Ti exhibits insignificant electrochemical activity and does not participate in the redox processes during the charge and discharge. In contrast, Ni, Fe, Co, and Cu show contributions around the Fermi level, indicating their active role in electron transfer and electrochemical activity. Ni, in particular at the Fermi level, is significantly involved in charge compensation during the Na^+ extraction/insertion.[26] It is noteworthy that Mn primarily contributes to the stability and structural integrity of the system, as the peaks of Mn from −2.8 to −1.7 eV represent the elevated

ADVANCED
SCIENCE NEWS

www.advancedsciencenews.com

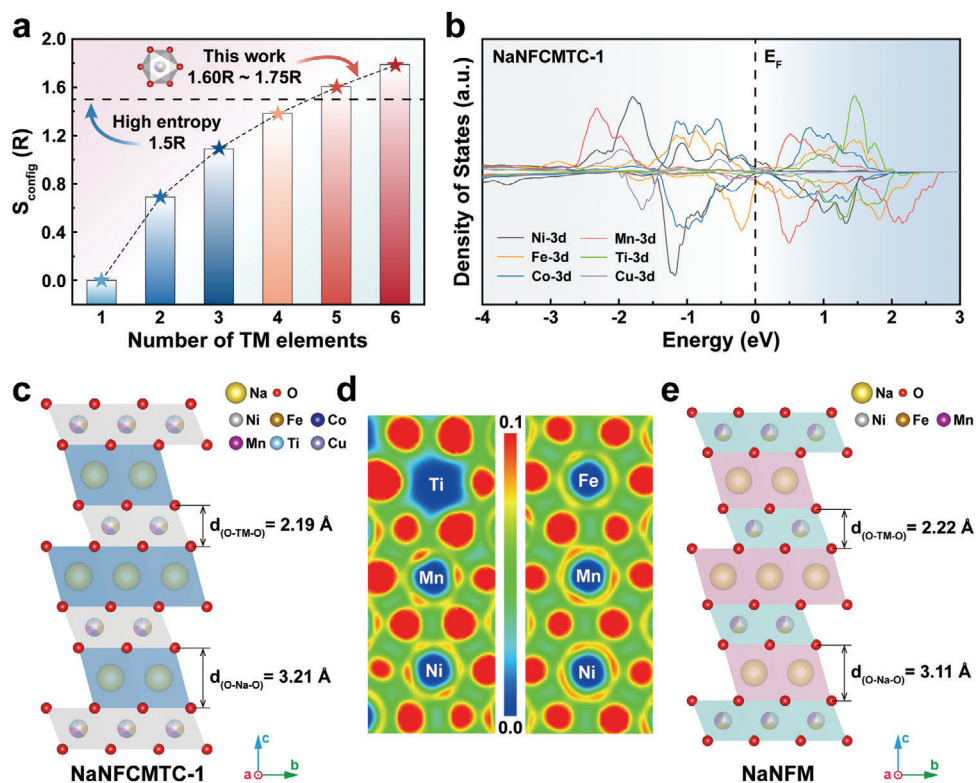**ADVANCED**
MATERIALS

www.advmat.de

Figure 1. Structural comparison between high-entropy and low-entropy sodium layered oxides. a) The relationship between configurational entropy and the number of transition metal elements. b) DOS calculation for NaNFCMTC-1. Schematic diagram of crystal structure and interlayer spacing for c) NaNFCMTC-1 and e) NaNFM. d) 2D slices of the charge density distribution for NaNFCMTC-1 (left) and NaNFM (right).

redox potential of $Mn^{4+/7+}$, which is typically not addressed in the investigation of cathodes for SIBs.

The crystal structure and interlayer spacing for NaNFCMTC-1 and $NaNi_{1/3}Fe_{1/3}Mn_{1/3}O_2$ (NaNFM) are schematically represented in Figure 1c and Figure 1e, which can be obtained from the refined results (Table S1 and Table S4, Supporting Information). The interlayer distance of $d_{(O—TM—O)}$ for NaNFCMTC-1 is 2.19 Å, 0.03 Å smaller than the $d_{(O—TM—O)}$ for NaNFM which is 2.22 Å. However, the $d_{(O—Na—O)}$ of NaNFCMTC-1 (3.21 Å) is 0.10 Å larger than that of NaNFM (3.11 Å). To understand this phenomenon, the electronic local function (ELF) for the structures of NaNFCMTC-1 and NaNFM was evaluated, as depicted in Figure 1d. The electron localization around oxygen increases after the substitution of transition metal ions, leading to a significant enhancement of the Ti—O bond, which establishes a stronger transition metal skeleton. This increase in electron localization also reduces the electron density between Na—O,[19] thereby minimizing the electrostatic interaction between electrons and interlayer sodium ions, facilitating the rapid diffusion kinetics of Na$^+$ within the system.

X-ray diffraction (XRD) and Rietveld refinement were performed to characterize the crystalline structures of the compounds which were synthesized through a solid-state method. The results reveal the O3-type stacking crystallization, belonging to the R3̄m space group, where all the cations are located at *3b* site with a random distribution (**Figures** 2a and S1, Supporting Information), and the detailed refined crystallographic parameters are

summarized in Table S1–S6 (Supporting Information). For five high-entropy materials, scanning electron microscopy (SEM) was conducted to investigate the morphological structure, where all the samples exhibit irregular granules within 10 µm (Figure 2a inset and Figure S2, Supporting Information). The actual chemical compositions of the high-entropy compounds were confirmed by inductively coupled plasma mass spectrometer (ICP-MS), and the results were similar to the designed values (Table S7–S11, Supporting Information).

The precise atomic-level structural information of NaNFCMTC-1 was revealed by scanning transmission electron microscopy (STEM) with annular bright-field (ABF) and high angle annular dark-field (HAADF). In the ABF image (Figure 2c), the columns of abvious dark-dot represent TM (Ni, Fe, Co, Mn, Ti, and Cu) layers and the columns of lighter dark-dot correspond to sodium layers, which is opposite in the HAADF image (Figure 2d).[27] From the [010] zone axis, ABCABC-stacking layered arrangements of atoms are clearly observed, corresponding to O3 structure. The distance between TM layers in a unit cell measured from the HAADF image is 16.19 Å, well consistent with the *c* value of the refined crystallographic data. The selected area electron diffraction (SAED) patterns of NaNFCMTC-1 combined with the bright field images clearly show the hexagonal arrangement on the direction of [001] zone axis (Figure 2b and Figure S3a, Supporting Information) as well as the layered structure on the direction of [11̄0] (Figure 2e) and [010] (Figure S3b, Supporting Information)

ADVANCED
SCIENCE NEWS

www.advancedsciencenews.com

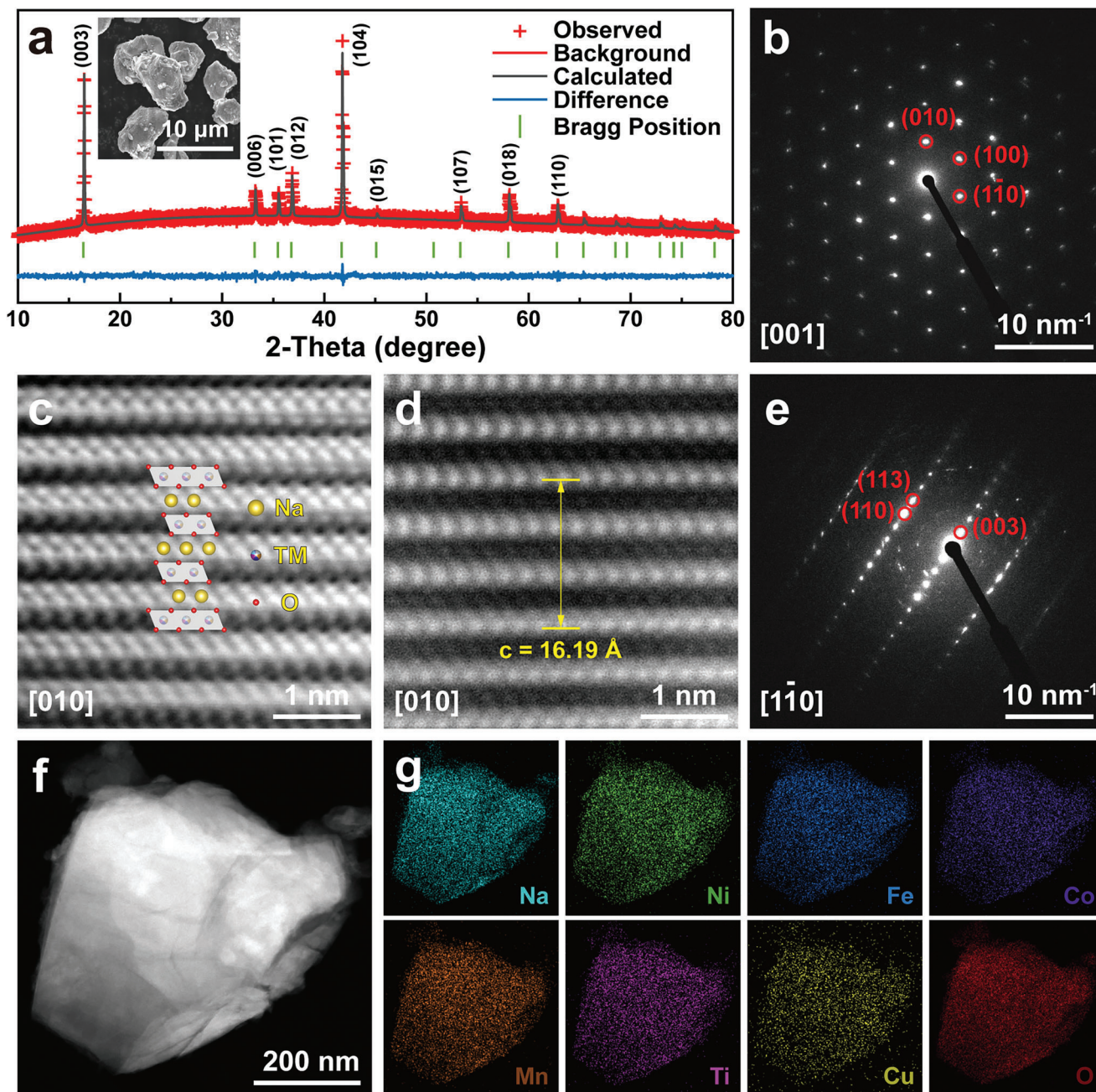**ADVANCED**
MATERIALS

www.advmat.de

Figure 2. Structure characterization of pristine NaNFCMTC-1 powder. a) Rietveld refinement of XRD pattern, the inset shows the SEM image. SAED patterns projected from the zone axis of b) [001] and e) [1$\bar{1}$0] directions. c) ABF-STEM and d) HADDF-STEM image at the [010] zone axis. f) TEM image and the corresponding g) EDS elemental mappings of Na, Ni, Fe, Co, Mn, Ti, Cu, and O.

zone axis. Figure S4 (Supporting Information) exhibits the high-resolution transmission electron microscopy (HRTEM) images of NaNFCMTC-1, where the interplanar distance is measured to be 5.39, 2.53, 2.45 and 2.16 Å, respectively, corresponding to the (003), (101), (012) and (104) lattice plane of O3 phase. The uniform distribution for the elements of Na, Ni, Fe, Co, Mn, Ti, Cu, and O is demonstrated using energy-dispersive spectroscopy (EDS) elemental mapping (Figure 2f–g and Figure S5, Supporting Information). To determine the valence states of each transition metal element in NaNFCMTC-1, X-ray photoelectron

spectroscopy (XPS) measurements were performed for the fresh powder, where the result of Ni^{2+}, Fe^{3+}, Co^{3+}, Mn^{4+}, Ti^{4+}, and Cu^{2+} is consistent with the expected oxidation states (Figure S6, Supporting Information).[28]

The electrochemical performance was evaluated using Na metal as anode in half cells. $Na_{0.9}Ni_{0.2}Fe_{0.2}Co_{0.2}Mn_{0.2}Ti_{0.2}O_2$ (NaNFCMTC-0′) and $Na_{0.9}Ni_{0.2}Fe_{0.2}Co_{0.2}Mn_{0.2}Ti_{0.1}Cu_{0.1}O_2$ (NaNFCMTC-2′) are selected for comparison to balance the influence of Na content on the performance of cathodes. Galvanostatic charge/discharge (GCD) curves of five samples at a
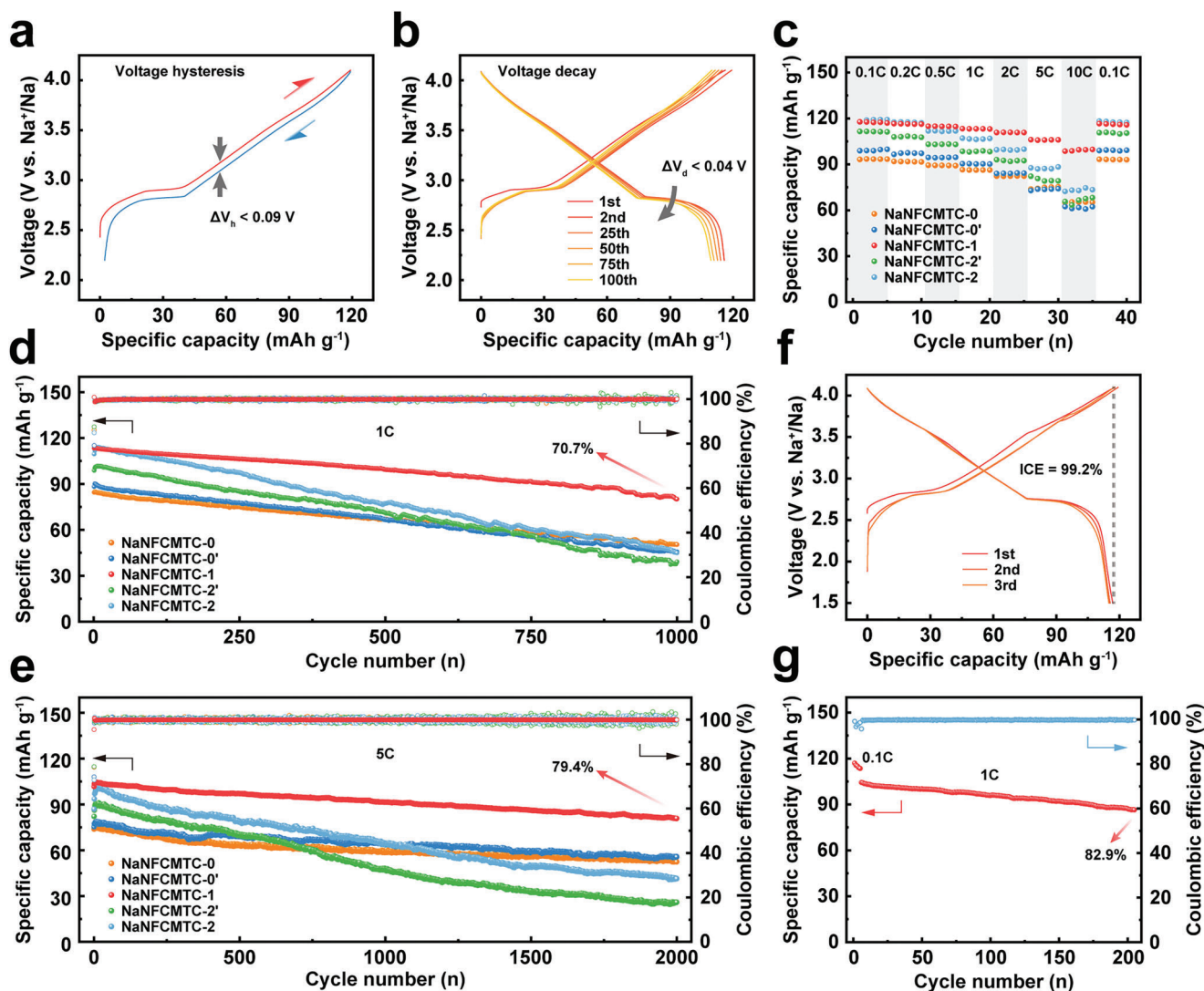
**ADVANCED
SCIENCE NEWS**

www.advancedsciencenews.com

**ADVANCED
MATERIALS**

www.advmat.de

Figure 3. Electrochemical performance of NaNFCMTC-1 cathode. a) Galvanostatic charge–discharge curves at 0.1 C. b) Voltage decay within 100 cycles at 0.1 C. c) Rate performance of five cathodes at different current densities. Long-term cycling performance of five cathodes at d) 1 C rate and e) 5 C rate. f) The initial three charge–discharge curves of NaNFCMTC-1‖HC full-cell at 0.1 C. g) Cycling performance of the full cell at 1 C.

current density of 0.1 C (1 C = 220 mA g^{-1}) within the voltage range of 2.2–4.1 V (vs. Na$^+$/Na) are shown in Figure S7 (Supporting Information). The NaNFCMTC-0, NaNFCMTC-0′, NaNFCMTC-1, NaNFCMTC-2′, and NaNFCMTC-2 exhibit initial discharge capacities of 93.2, 98.9, 117.8, 111.5, and 117.7 mAh g^{-1}, respectively. NaNFCMTC-1 achieves superior reversibility with a high initial Coulombic efficiency (ICE) of 99.7%, while the other four samples (NaNFCMTC-0, NaNFCMTC-0′, NaNFCMTC-2′, and NaNFCMTC-2) get ICEs of 92.9%, 87.3%, 92.5%, and 90.6%, respectively. As a consequence, the voltage hysteresis of NaNFCMTC-1 is less than 0.09 V (**Figure 3a**). When the cutoff voltage comes to 4.3 V, a significant voltage hysteresis reaches 0.23 V due to the phase transition in the high voltage region beyond 4.2 V (Figure S8, Supporting Information). During 100 cycles at 0.1 C, the average working voltage remains ≈3.20 V (Figure S9, Supporting Information), and the overall voltage decay is only 0.04 V (Figure 3b), with a capacity retention

of 94.5% (Figure S10, Supporting Information) in the voltage range of 2.2–4.1 V. From the suppressed voltage hysteresis and voltage decay, it can be inferred that high-entropy structure might inhibit cation migration and enhance the reversibility of redox reactions, thus achieving a highly reversible phase transition.

Rate capability at various current densities was further investigated (Figure 3c). NaNFCMTC-1 delivers discharge capacities of 117.4, 116.6, 114.9, 113.3, 110.8, 106.1, and 98.6 mAh g^{-1} at 0.1, 0.2, 0.5, 1, 2, 5, and 10 C rates, respectively, maintaining 84.0% capacity ratio of 10 C to 0.1 C, which is most exceptional among the five high-entropy cathodes. When it comes back to 0.1 C, the capacity of 116.6 mAh g^{-1} can be still obtained by NaNFCMTC-1, almost back to the initial state, revealing its outstanding structural stability and accelerated transport kinetics of sodium ions. For long-term cycling performance, NaNFCMTC-0, NaNFCMTC-0′, NaNFCMTC-1, NaNFCMTC-2′, and NaNFCMTC-2 exhibit

**ADVANCED
SCIENCE NEWS**

www.advancedsciencenews.com
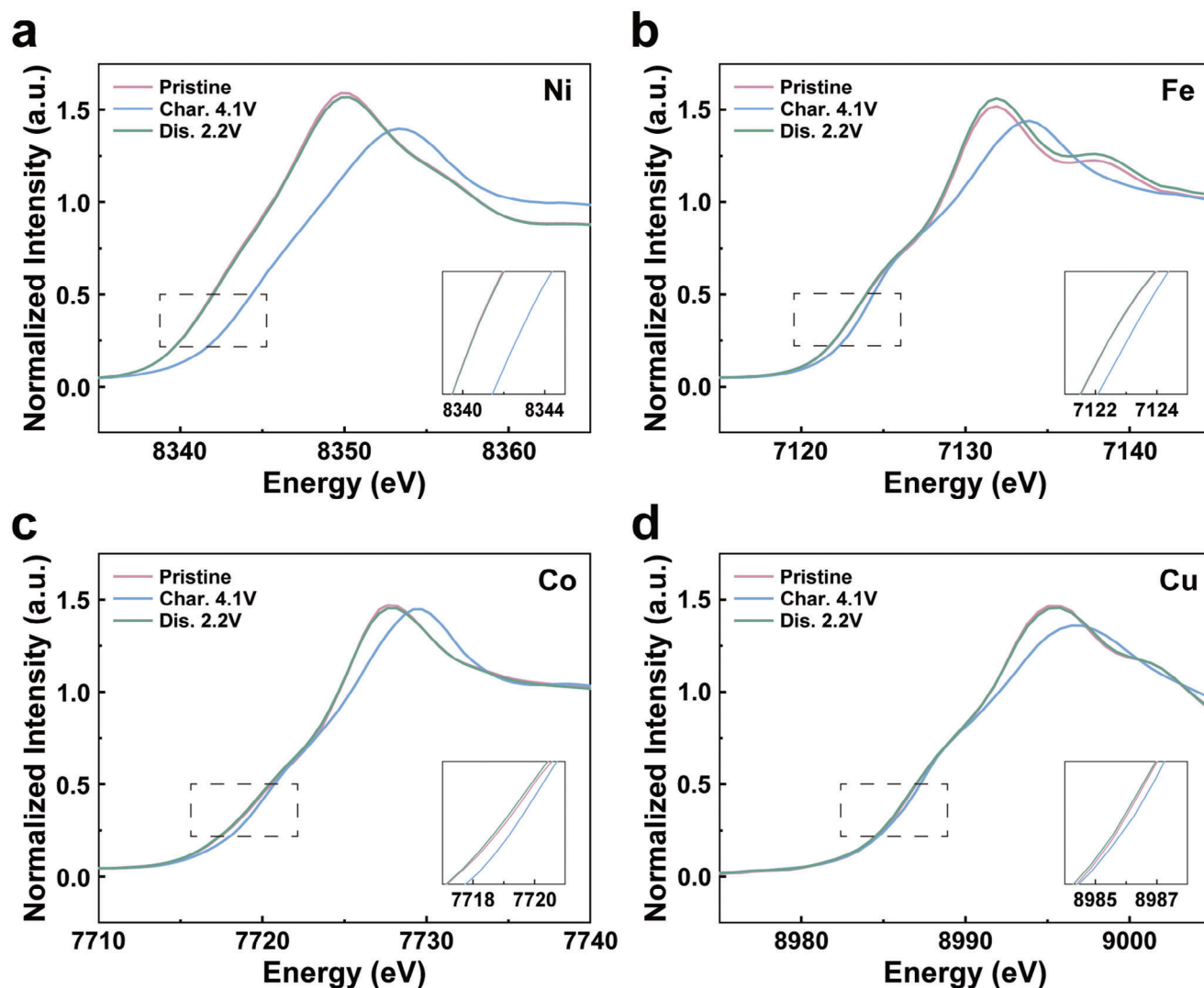
**ADVANCED
MATERIALS**

www.advmat.de

Figure 4. Charge compensation mechanism of NaNFCMTC-1 cathode during sodium (de)intercalation. Normalized ex situ XANES spectra of a) Ni K-edge, b) Fe K-edge, c) Co K-edge, and d) Cu K-edge at pristine, fully charged (4.1 V), and fully discharged (2.2 V) states.

capacities of 50.3, 45.6, 80.1, 39.1, and 44.9 mAh g^{-1} after 1000 cycles at 1 C, corresponding to the retentions of 59.4%, 51.6%, 70.7%, 39.6%, and 41.0%, respectively (Figure 3d). Particularly, because of high average efficiency of Na||Na cell and the sufficient sodium anode (Figures S11 and S12, Supporting Information), NaNFCMTC-1 still gains a capacity of 80.8 mAh g^{-1} even at the high current density of 5 C (1100 mA g^{-1}) after 2000 cycles,[29] which is equivalent to the capacity retention of 79.4% (Figure 3e). NaNFCMTC-1 also delivers satisfactory fast-charge and slow-discharge performance as well as good cycle stability and rate capability with high mass loading (Figures S13 and S14, Supporting Information). This indicates that rationally high-entropy regulated transition metal ions improve the rigidity of the framework, and thus enhance the structural stability during the repeated Na$^+$ (de)intercalation process. The performance of O3-type high-entropy cathodes reported recently is summarized in Table S12 (Supporting Information), where our work manifests significant advantages.

Full cells with NaNFCMTC-1 cathode and presodiated hard carbon (HC) anode (Figure S15a, Supporting Information), were assembled to demonstrate practicability. As shown in Figure 3f, the NaNFCMTC-1||HC full-cell exhibits a pretty high ICE of 99.2% with a reversible capacity of 116.9 mAh g^{-1}, enabling the average operating voltage to reach about 3.1 V accompanied by an energy density of 265.8 Wh kg^{-1} (calculated based on the total loading mass of cathode and anode). Due to the inferior rate performance of HC, the full cell shows capacity decay continuously at relatively high current densities, but it can still deliver a stable capacity of 98.3 mAh g^{-1} at the rate of 2 C (Figure S15b, Supporting Information). Nevertheless, the full cell obtains a capacity retention of 82.9% after 200 cycles at the rate of 1 C (Figure 3g), which suggests the promising application potential for high-entropy NaNFCMTC-1 cathode.

In order to preliminarily investigate the redox reactions in high-entropy system, the cyclic voltammetry (CV) measurements were carried out at the scan rate of 0.1 mV s^{-1} for the five
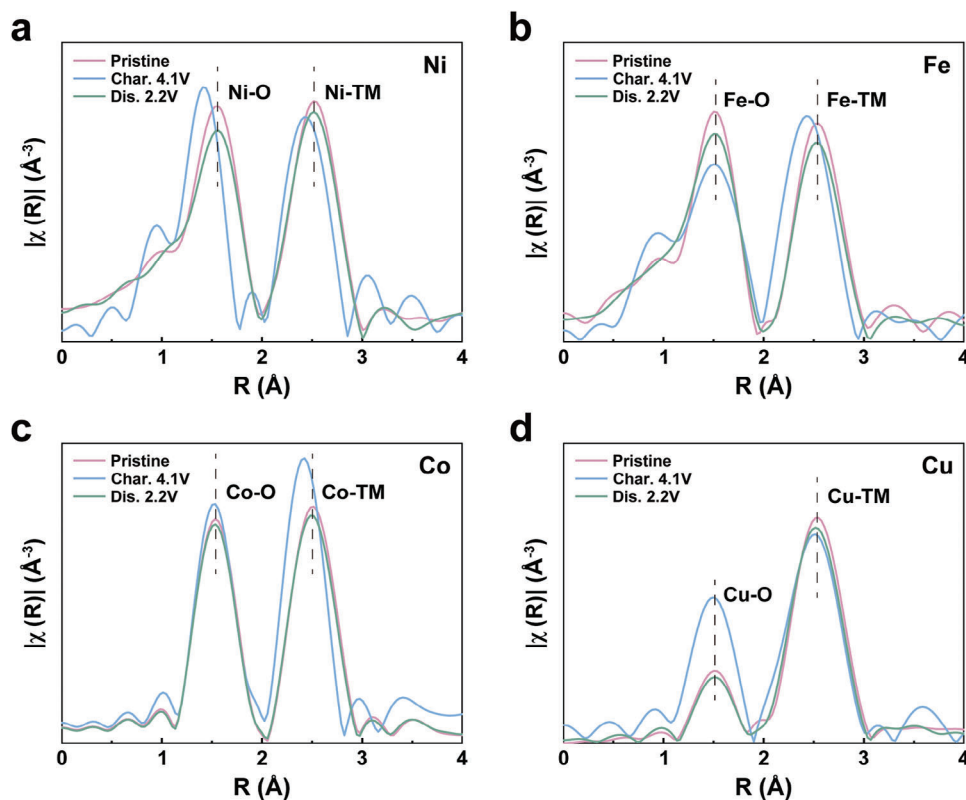
Figure 5. Coordination environment changes of NaNFCMTC-1 cathode during sodium (de)intercalation. Ex situ EXAFS spectra for a) Ni K-edge, b) Fe K-edge, c) Co K-edge, and d) Cu K-edge at pristine, fully charged (4.1 V), and fully discharged (2.2 V) states.

cathodes (Figure S16, Supporting Information). All these curves are smooth with only two pairs of redox peaks at ≈2.7–3.0 and 3.5–3.8 V, respectively. Based on the DOS result, the obvious peaks at 2.7–3.0 V may be the redox of nickel because of the dominant position of Ni, which is also related to the O3–P3 phase transition. The less pronounced peaks at 3.5–3.8 V can be assigned to the redox couples of Fe^{3+}/Fe^{4+}, Co^{3+}/Co^{4+}, and Cu^{2+}/Cu^{3+}, given their electrochemical activity. It is worth noting that the intensity of the redox peaks for nickel in NaNFCMTC-1, NaNFCMTC-2′, and NaNFCMTC-2 is higher than that in NaNFCMTC-0 and NaNFCMTC-0′, while the intensity for the redox peaks at 3.5–3.8 V are similar in five samples, suggesting that the addition of Cu might promote the Ni redox reaction in the system, thereby increasing the electrochemical capacity. The excellent redox reversibility in high-entropy cathodes is achieved, as all the CV curves for each sample show a high degree of coincidence.

Ex situ X-ray absorption near edge structure (XANES) was performed to further understand the charge compensation mechanism in NaNFCMTC-1. From the previous DOS analysis and XPS results, tetravalent Mn^{4+} and Ti^{4+} have no electrochemical activity in our selected testing voltage range,[30] so we only characterize the remaining transition metal elements Ni, Fe, Co, and Cu. Comparing the position of K-edge for NaNFCMTC-1 electrode in pristine state with the reference compounds (NiO, Fe_2O_3, Co_3O_4, and CuO), the valence states of Ni^{2+}, Fe^{3+}, Co^{3+}, and Cu^{2+} are further identified (Figure S17, Supporting Information), which is in good agreement with XPS results. During the charge process (Na$^+$ extraction), the Ni K-edge (**Figure** 4a) shifts more than

2 eV toward the higher energy, which may indicate the complete oxidation of Ni^{2+} to Ni^{4+}, considering ≈117 mAh g^{-1} capacity of NaNFCMTC-1. Meanwhile, the K-edge spectra of Fe, Co, and Cu only exhibit a slight edge shift (Figure 4b–d), indicating the partial oxidation of Fe^{3+}/Fe^{4+}, Co^{3+}/Co^{4+}, and Cu^{2+}/Cu^{3+}. Upon the discharge process (Na$^+$ insertion), the absorption edge of Ni moves to lower energy and finally returns to the pristine position at the fully discharged state, suggesting the redox of Ni^{2+}/Ni^{4+} is completely reversible during the electrochemical process in NaNFCMTC-1, corresponding to a specific capacity of 96 mAh g^{-1}. In the same way, the absorption edges of Fe, Co, and Cu shift back to the initial position, delivering ≈21 mAh g^{-1} discharge capacity.

Extended X-ray Absorption Fine Structure (EXAFS) at different electrochemical states can be obtained through Fourier-transform (**Figure** 5), where the first peak at about 1.5 Å represents the TM—O coordination shell and the second peak at about 2.5 Å is attributed to the TM—TM coordination shell. The variation in the coordination environment can be easily observed from the position and intensity of peaks in EXAFS spectra.[31] At the fully charged state, the TM—O bonds of the four cations become shorter based on their charge compensation contribution due to oxidation, where the length of Ni—O bond changes most prominently, while the variation in Fe—O, Co—O, and Cu—O bonds is not obvious. The intensities of the Ni—O, Co—O, and Cu—O bonds increase while a decrease is observed for the intensity of Fe—O bond after charge, which can be attributed to Fe^{4+} by its Jahn-Teller distortion.[28c] Cu—O undergoes significant changes

**ADVANCED
SCIENCE NEWS**

www.advancedsciencenews.com

**ADVANCED
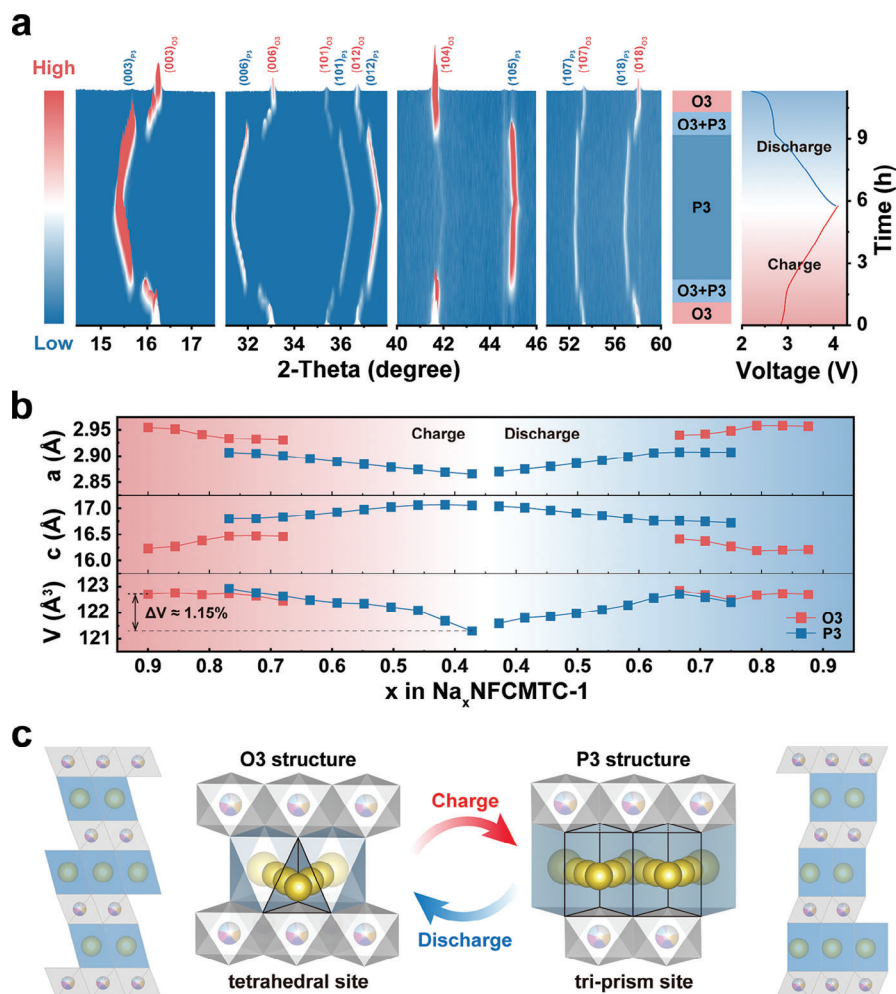MATERIALS**

www.advmat.de

Figure 6. Structural evolution during electrochemical sodium extraction/insertion of NaNFCMTC-1 cathode. a) In situ XRD patterns corresponding voltage profile during the first charge–discharge at 0.1 C in the voltage range of 2.2–4.1 V. b) Evolution of lattice parameters (*a*-axis, *c*-axis, and volume) calculated from the in situ XRD data. c) Schematic diagram of O3 and P3 structure with their sodium ion transport channels.

in intensity but minimal changes in length, indicating that a stronger redox reaction occurred around it, proving the excitation of Cu on the reaction activity of the system. Based on the XANES and EXAFS results, the redox reaction in NaNFCMTC-1 cathode is highly reversible, in which Ni significantly contributes to capacity while Fe and Co dedicate partially, Cu provides a little charge compensation but stimulates the reactivity. The excellent stability of the NaNFCMTC-1 can be assigned to the structural pillars served by the inactive elements (Mn and Ti) in TM layers during sodium extraction/insertion.[32]

To investigate the structural evolution upon electrochemical Na+ (de)intercalation, in situ XRD measurements were conducted on the first cycle of NaNFCMTC-1 cathode (**Figure 6a**), where the diffraction peak of aluminum foil at $2\theta = 44.6°$ is invariant. Upon Na+ extraction, shifting toward a lower angle can be observed for the (003) and (006) peaks, indicating the increase of lattice parameter *c* due to the interlayer expansion which is caused by the enhanced electrostatic repulsion of O2−. Furthermore, the (101) and (012) peaks move to a higher angle, suggesting that the reduced radius of oxidized ions shrinks the inter-

planar spacing, leading to the decrease of lattice parameter *a*. When the extraction of Na+ reaches 0.13, P3 phase with a space group of R3m starts appearing, implied by the generation of new peaks of (003) and (006) at a lower position with the peaks of (101), (012), and (105) at a higher position. There is a coexistence of O3 and P3 phases in the region of $0.68 \leq x \leq 0.77$, after which the diffraction peaks of O3 phase disappear, indicating the complete conversion from O3 to P3 phase at 0.22 extraction of Na+. The reflections of P3 phase continuously shift without any new peaks appearing until the end of charge, demonstrating a solid-solution reaction. During discharge, as the sodium ions are inserted constantly, all the diffraction peaks undergo an opposite process and eventually return to the initial O3 state. The changes of XRD patterns during charge–discharge obtain a high degree of symmetry, indicating that modulating configurational entropy stabilizes the transition metal skeleton, thus achieving a highly reversible phase transition of O3–P3–O3.

Corresponding lattice parameters were acquired by refining the in situ XRD data using Rietveld method (Figure 6b), where the tendency is in good agreement with the analysis. The
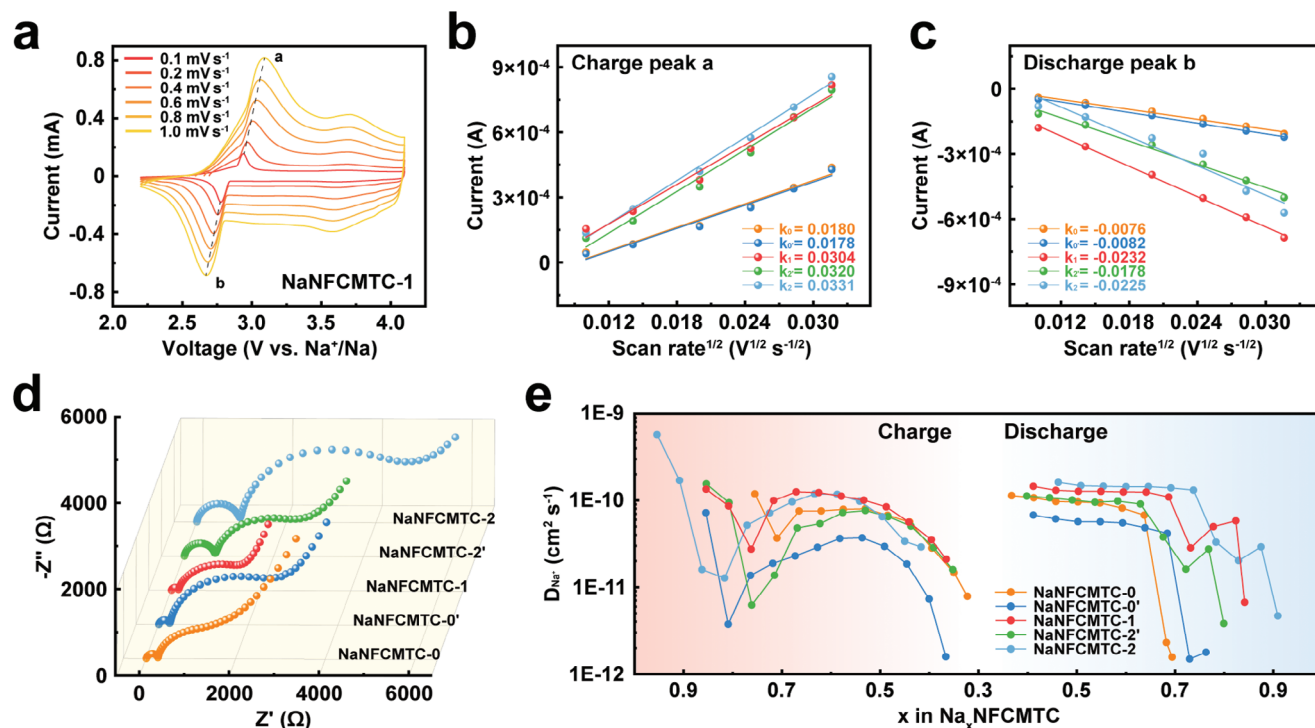
Figure 7. Investigations on kinetics performance of Na$^+$ transfer. a) CV curves of NaNFCMTC-1 within the voltage range of 2.2–4.1 V at different scan rates from 0.1 to 1.0 mV s^{-1}. Corresponding linear relationship of peak currents with the square root of scan rate on b) peak **a** for charge process and c) peak **b** for discharge process. d) EIS plots of the cathodes at the fully discharged state after five cycles. e) Na$^+$ diffusion coefficients during the first charge–discharge processes calculated from GITT measurements.

significant increase and decrease for lattice parameters c and a can be observed during the forming of P3 phase, which is linked to the gliding of TMO$_2$ slabs caused by O3–P3 phase transition.[33] The increased lattice parameter c in P3 phase means the expansion of interlayer spacing, which accelerates the transport of sodium ions. It is worth noting that the P3 phase occurs at the sodium ion extraction ≈0.13, and rapidly transitions into the complete P3 phase thereafter until the late stage of discharge, which makes NaNFCMTC-1 cathode maintain a wider range in P phase of the tri-prism structure with fast Na$^+$ kinetics rather than O phase of the octahedral structure with poor Na$^+$ kinetics during electrochemical cycling (Figure 6c),[34] contributing to its excellent rate capability. Moreover, compared with the initial state, the volume change of the unit cell at the fully charged state is only 1.15%, revealing remarkable structural stability of the high-entropy cathode, which accounts for the high capacity retention during long-term cycling.

In view of the outstanding rate performance exhibited by the cathodes, CV tests were performed at different scan rates from 0.1 to 1.0 mV s^{-1} to make a quantitative comparison of Na$^+$ transport capacity. The most obvious redox peaks are selected for calculation (**Figures 7a** and S18, Supporting Information), where peak **a** and peak **b** represent the typical sodium ion diffusion in the charge and discharge stages, respectively. The linear relationship of peak currents with the square root of scan rate was fitted due to the positive correlation between D$_{Na+}$ and the slope of the I$_p$/v$^{1/2}$ curves (Figure 7b,c). The Cu containing cathodes (NaNFCMTC-1, NaNFCMTC-2′, and NaNFCMTC-2) are deter-

mined to have higher absolute slope values with larger apparent Na$^+$ diffusion coefficients (Table S13, Supporting Information) than the cathodes without Cu (NaNFCMTC-0 and NaNFCMTC-0′) both at peaks **a** and **b**, indicating that the addition of Cu not only stimulates the redox activity in the system but also promotes the kinetics of sodium ions. Electrochemical impedance spectroscopy (EIS) was conducted to get an insight view of Na$^+$ diffusion impedance (Figure 7d), and the results were fitted using the equivalent circuit in Figure S19 (Supporting Information). Both Nyquist plots (Figure S20, Supporting Information) and impedance results (Table S14, Supporting Information) indicate the least overall resistance of NaNFCMTC-1, which is also demonstrated to obtain the lowest R_w, suggesting the excellent diffusion performance of Na$^+$ inside the material.[35]

Galvanostatic intermittent titration technique (GITT) measurements were performed to further understand the sodium ion diffusion throughout the whole charge and discharge process (Figure S21, Supporting Information), from which the diffusion coefficient of Na$^+$ at different states can be calculated (Figure 7e). Along with the charge progressing, there is an obvious drop occurring on each curve, corresponding to the phase transition of O3–P3. As the materials completely convert into P3 phase, the diffusion rates of Na$^+$ increase. During discharge, P3 structure provides a good diffusion channel for sodium ions until the cathodes undergo a phase transition and return to O3 phase. It should be explained that there is a decrease in diffusion coefficient upon the end of the charge state, which is not related to the P3 structure, but caused by the weakening of electrostatic
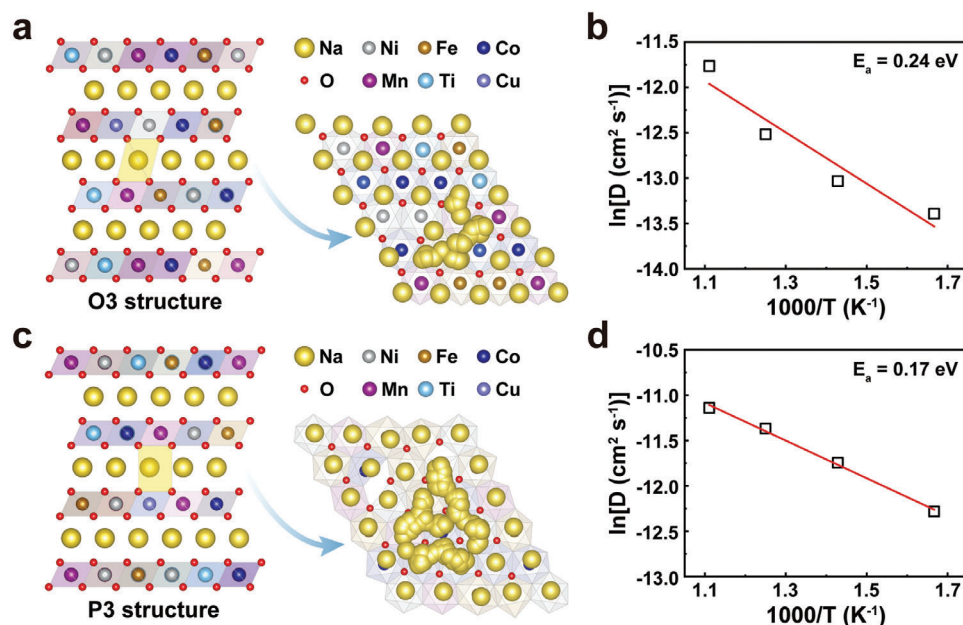
Figure 8. Na^+ kinetics of NaNFCMTC-1 revealed by FPMD simulations. Trajectories of sodium ions at 900 K from 2 to 8 ps in a) O3 and c) P3 phase. The right panel provides a top view of the Na^+ layer. Corresponding Arrhenius plots of diffusion coefficients in NaNFCMTC-1 are presented in b) O3 and d) P3 phase, from which Na^+ migration energy barriers of 0.24 and 0.17 eV are obtained, respectively.

repulsion of Na—Na as the diminution of sodium concentration in the lattice.[19] The voltage polarization (Figure S22a,b, Supporting Information) and Ohmic polarization (Figure S22c,d, Supporting Information) during the charge–discharge process can also be acquired from GITT data, where NaNFCMTC-1 exhibits a lower polarization compared to others, corresponding to its inconspicuous voltage hysteresis.

To gain a more profound understanding of the diffusion dynamics of NaNFCMTC-1, first-principles molecular dynamics (FPMD) calculations were employed for both O3-type and P3-type phases. The mean square displacement (MSD) curves, extracted from stable data covering the time span of 2 to 8 ps (Figures S23 and S24, Supporting Information), demonstrate minimal variations in the motion of ions, excluding Na^+, across the temperature range of 600 to 900 K. This suggests remarkable thermal stability with the high-entropy framework of both O3 and P3 structures, effectively impeding the migration of cations and mitigating voltage hysteresis. In contrast, Na^+ exhibits substantial diffusion, with a noticeable increase at elevated temperatures, as evidenced by the diffusion coefficient D_{Na^+} derived from the slope of the MSD curves. Furthermore, **Figure 8a** and Figure 8c emphasize a notable disparity in Na^+ diffusion behavior between O3 and P3 phases. In the O3-type, Na^+ permeates adjacent sodium sites through tetrahedral vacancies located between octahedra, while in the P3-type configuration, it traverses 2D channels within tri-prisim sites.[36] Simultaneously, Figure 8b and Figure 8d reveal a lower diffusion barrier (0.17 eV) and a significantly higher diffusion coefficient (1.49 $\times$ 10^{-8} cm^2 s^{-1}) at 300 K for the P3 phase compared to the O3 phase (0.24 eV, 1.19 $\times$ 10^{-8} cm^2 s^{-1}), as deduced from the Arrhenius equation,[37] which augurs well for the fast sodium ion diffusion. Therefore, the transition of NaNFCMTC-1 from the O3 phase to the P3 phase results in superior Na^+ kinetic

performance without compromising the thermal stability of the system.

3. Conclusion

In summary, a series of high-entropy layered oxides were selected and synthesized toward application for SIBs. The high-entropy configuration within transition metal slabs helps to regulate electronic structure, strengthen TMO_2 skeleton and enlarge the sodium ion diffusion channel, leading to the higher reversibility of TM redox, more mitigatory phase evolution from O3 to P3 phase, lower Na^+ migration energy barrier of 0.17 eV, thus faster sodium ions diffusion ($\approx 10^{-10}$ cm^2 s^{-1}) during Na^+ (de)intercalation process. Therefore, suppression of voltage hysteresis, enhancement of rate capability and prolongment of cycling stability for this high-entropy material are achieved in SIBs. The target NaNFCMTC-1 material exhibits a very small voltage hysteresis of 0.09 V, $\approx 80\%$ of capacity retention after 2000 cycles and a distinguished rate capability with almost 84% of capacity retention at 10 C. This work highlights the significance of high-entropy configuration design within TMO_2 layers of the layered oxide cathode materials for SIBs, which will undoubtedly facilitate their future implementation in practical applications.

Supporting Information

Supporting Information is available from the Wiley Online Library or from the author.

Conflict of Interest

The authors declare no conflict of interest.

Data Availability Statement

The data that support the findings of this study are available from the corresponding author upon reasonable request.

Keywords

[1] a) X. Xiang, K. Zhang, J. Chen, *Adv. Mater.* **2015**, *27*, 5343; b) M. Chen, Q. Liu, S.-W. Wang, E. Wang, X. Guo, S.-L. Chou, *Adv. Energy Mater.* **2019**, *9*, 1803609; c) D. Lan, X. Qu, Y. Tang, L. Liu, J. Liu, *J. Electrochem.* **2022**, *28*, 55.

[2] a) C. Vaalma, D. Buchholz, M. Weil, S. Passerini, *Nat. Rev. Mater.* **2018**, *3*, 18013; b) X. Liang, J.-Y. Hwang, Y.-K. Sun, *Adv. Energy Mater.* **2023**, *13*, 2301975; c) H.-R. Yao, L. Zheng, S. Xin, Y.-G. Guo, *Sci China Chem* **2022**, *65*, 1076.

[3] P.-F. Wang, Y. You, Y.-X. Yin, Y.-G. Guo, *Adv. Energy Mater.* **2018**, *8*, 1701912.

[4] Q. Liu, Z. Hu, M. Chen, C. Zou, H. Jin, S. Wang, S.-L. Chou, S.-X. Dou, *Small* **2019**, *15*, 1805381.

[5] a) A. Joshi, S. Chakraborty, S. H. Akella, A. Saha, A. Mukherjee, B. Schmerling, M. Ejgenberg, R. Sharma, M. Noked, *Adv. Mater.* **2023**, *35*, 2304440; b) J.-Y. Hwang, S.-T. Myung, Y.-K. Sun, *Chem. Soc. Rev.* **2017**, *46*, 3529.

[6] a) Y. Xie, H. Wang, G. Xu, J. Wang, H. Sheng, Z. Chen, Y. Ren, C.-J. Sun, J. Wen, J. Wang, D. J. Miller, J. Lu, K. Amine, Z.-F. Ma, *Adv. Energy Mater.* **2016**, *6*, 1601306; b) S. Komaba, N. Yabuuchi, T. Nakayama, A. Ogata, T. Ishikawa, I. Nakai, *Inorg. Chem.* **2012**, *51*, 6211; c) N. A. Katcho, J. Carrasco, D. Saurel, E. Gonzalo, M. Han, F. Aguesse, T. Rojo, *Adv. Energy Mater.* **2017**, *7*, 1601477.

[7] P.-F. Wang, H.-R. Yao, X.-Y. Liu, J.-N. Zhang, L. Gu, X.-Q. Yu, Y.-X. Yin, Y.-G. Guo, *Adv. Mater.* **2017**, *29*, 1700210.

[8] T. Chen, B. Ouyang, X. Fan, W. Zhou, W. Liu, K. Liu, *Carbon Energy* **2022**, *4*, 170.

[9] H.-R. Yao, W.-J. Lv, Y.-X. Yin, H. Ye, X.-W. Wu, Y. Wang, Y. Gong, Q. Li, X. Yu, L. Gu, Z. Huang, Y.-G. Guo, *ACS Appl. Mater. Interfaces* **2019**, *11*, 22067.

[10] T.-Y. Yu, H.-H. Ryu, G. Han, Y.-K. Sun, *Adv. Energy Mater.* **2020**, *10*, 2001609.

[11] H. Fu, G. Fan, J. Zhou, X. Yu, X. Xie, J. Wang, B. Lu, S. Liang, *Inorg. Chem.* **2020**, *59*, 13792.

[12] a) E. McCalla, M. T. Sougrati, G. Rousse, E. J. Berg, A. Abakumov, N. Recham, K. Ramesha, M. Sathiya, R. Dominko, G. Van Tendeloo, P. Novák, J.-M. Tarascon, *J. Am. Chem. Soc.* **2015**, *137*, 4804; b) W. He, W. Guo, H. Wu, L. Lin, Q. Liu, X. Han, Q. Xie, P. Liu, H. Zheng, L. Wang, X. Yu, D.-L. Peng, *Adv. Mater.* **2021**, *33*, 2005937.

[13] a) C. Cheng, C. Chen, S. Chu, H. Hu, T. Yan, X. Xia, X. Feng, J. Guo, D. Sun, J. Wu, S. Guo, L. Zhang, *Adv. Mater.* **2022**, *34*, 2201152; b) N. Voronina, M.-Y. Shin, H.-J. Kim, N. Yaqoob, O. Guillon, S. H. Song, H. Kim, H.-D. Lim, H.-G. Jung, Y. Kim, H.-K. Lee, K.-S. Lee, K. Yazawa, K. Gotoh, P. Kaghazchi, S.-T. Myung, *Adv. Energy Mater.* **2022**, *12*, 2103939.

[14] F. Li, R. Liu, J. Liu, H. Li, *Adv. Funct. Mater.* **2023**, *33*, 2300602.

[15] H. Ren, Y. Li, Q. Ni, Y. Bai, H. Zhao, C. Wu, *Adv. Mater.* **2022**, *34*, 2106171.

[16] a) K. Kubota, T. Asari, S. Komaba, *Adv. Mater.* **2023**, *35*, 2300714; b) A. Sarkar, Q. Wang, A. Schiele, M. R. Chellali, S. S. Bhattacharya, D. Wang, T. Brezesinski, H. Hahn, L. Velasco, B. Breitung, *Adv. Mater.* **2019**, *31*, 1806236; c) X.-Y. Du, Y. Meng, H. Yuan, D. Xiao, *Energy Storage Mater.* **2023**, *56*, 132.

[17] E. P. George, D. Raabe, R. O. Ritchie, *Nat. Rev. Mater.* **2019**, *4*, 515.

[18] F. Ding, H. Wang, Q. Zhang, L. Zheng, H. Guo, P. Yu, N. Zhang, Q. Guo, F. Xie, R. Dang, X. Rong, Y. Lu, R. Xiao, L. Chen, Y.-S. Hu, *J. Am. Chem. Soc.* **2023**, *145*, 13592.

[19] H. Wang, X. Gao, S. Zhang, Y. Mei, L. Ni, J. Gao, H. Liu, N. Hong, B. Zhang, F. Zhu, W. Deng, G. Zou, H. Hou, X.-Y. Cao, H. Chen, X. Ji, *ACS Nano* **2023**, *17*, 12530.

[20] F. Ding, C. Zhao, D. Xiao, X. Rong, H. Wang, Y. Li, Y. Yang, Y. Lu, Y.-S. Hu, *J. Am. Chem. Soc.* **2022**, *144*, 8286.

[21] J.-L. Yue, W.-W. Yin, M.-H. Cao, S. Zulipiya, Y.-N. Zhou, Z.-W. Fu, *Chem. Commun.* **2015**, *51*, 15712.

[22] C. Zhao, F. Ding, Y. Lu, L. Chen, Y.-S. Hu, *Angew. Chem., Int. Ed.* **2020**, *59*, 264.

[23] J.-Y. Hwang, C. S. Yoon, I. Belharouak, Y.-K. Sun, *J. Mater. Chem. A* **2016**, *4*, 17952.

[24] Q. Wang, S. Mariyappan, J. Vergnet, A. M. Abakumov, G. Rousse, F. Rabuel, M. Chakir, J.-M. Tarascon, *Adv. Energy Mater.* **2019**, *9*, 1901785.

[25] A. Amiri, R. Shahbazian-Yassar, *J. Mater. Chem. A* **2021**, *9*, 782.

[26] K. Walczak, A. Plewa, C. Ghica, W. Zając, A. Trenczek-Zając, M. Zając, J. Toboła, J. Molenda, *Energy Storage Mater.* **2022**, *47*, 500.

[27] L. Yu, Z. Cheng, K. Xu, Y.-X. Chang, Y.-H. Feng, D. Si, M. Liu, P.-F. Wang, S. Xu, *Energy Storage Mater.* **2022**, *50*, 730.

[28] a) Y. Li, Z. Yang, S. Xu, L. Mu, L. Gu, Y.-S. Hu, H. Li, L. Chen, *Adv. Sci.* **2015**, *2*, 1500031; b) C. Wang, L. Liu, S. Zhao, Y. Liu, Y. Yang, H. Yu, S. Lee, G.-H. Lee, Y.-M. Kang, R. Liu, F. Li, J. Chen, *Nat. Commun.* **2021**, *12*, 2256; c) C.-C. Lin, H.-Y. Liu, J.-W. Kang, C.-C. Yang, C.-H. Li, H.-Y. T. Chen, S.-C. Huang, C.-S. Ni, Y.-C. Chuang, B.-H. Chen, C.-K. Chang, H.-Y. Chen, *Energy Storage Mater.* **2022**, *51*, 159.

[29] F. Fu, X. Liu, X. Fu, H. Chen, L. Huang, J. Fan, J. Le, Q. Wang, W. Yang, Y. Ren, K. Amine, S.-G. Sun, G.-L. Xu, *Nat. Commun.* **2022**, *13*, 2826.

[30] a) D. A. Anang, J.-H. Park, D. S. Bhange, M. K. Cho, W. Y. Yoon, K. Y. Chung, K.-W. Nam, *Ceram. Int.* **2019**, *45*, 23164; b) P. Zhou, Z. Che, J. Liu, J. Zhou, X. Wu, J. Weng, J. Zhao, H. Cao, J. Zhou, F. Cheng, *Energy Storage Mater.* **2023**, *57*, 618.

[31] L. Yao, P. Zou, C. Wang, J. Jiang, L. Ma, S. Tan, K. A. Beyer, F. Xu, E. Hu, H. L. Xin, *Adv. Energy Mater.* **2022**, *12*, 2201989.

[32] X. Gao, X. Zhang, X. Liu, Y. Tian, Q. Cai, M. Jia, X. Yan, *Small Methods* **2023**, *7*, 2300152.

[33] Y. Sun, S. Guo, H. Zhou, *Energy Environ. Sci.* **2019**, *12*, 825.

[34] Y. Shi, Z. Zhang, P. Jiang, A. Gao, K. Li, Q. Zhang, Y. Sun, X. Lu, D. Cao, X. Lu, *Energy Storage Mater.* **2021**, *37*, 354.

[35] J. Chen, G. Zou, W. Deng, Z. Huang, X. Gao, C. Liu, S. Yin, H. Liu, X. Deng, Y. Tian, J. Li, C. Wang, D. Wang, H. Wu, L. Yang, H. Hou, X. Ji, *Adv. Funct. Mater.* **2020**, *30*, 2004302.

[36] Q. Bai, L. Yang, H. Chen, Y. Mo, *Adv. Energy Mater.* **2018**, *8*, 1702998.

[37] N. Tian, Y. Gao, Y. Li, Z. Wang, X. Song, L. Chen, *Angew. Chem., Int. Ed.* **2016**, *55*, 644.